Supporting Information

Dominating Role of Ni^0 on the Interface of Ni/NiO for Enhanced Hydrogen Evolution Reaction

Jing Wang, Shanjun Mao, Zeyan Liu, Zhongzhe Wei, Haiyan Wang, Yiqing Chen, Yong Wang*

Advanced Materials and Catalysis Group, Center for Chemistry of High-performance and Novel Materials, Department of Chemistry, Zhejiang University, Hangzhou 310028, P. R. China.

*Corresponding Author: chemwy@zju.edu.cn

Table S1. The preparation parameters of different samples.

Samples	Melamine [g]	$Ni(NO_3)_2 \cdot 6H_2O$ [g]	Temperature [^oC]	Holding Time [h]
NiO_x@NC-700	20	1.11	700	1
NiO_x@BCNTs	20	1.11	700	2
NiO_x@NC-800	20	1.11	800	1
NiO_x@NC-900	20	1.11	900	1
NiO_x@NC-1000	20	1.11	1000	1
NiO	--	1.11	800	1

Table S2. Textural properties of the catalysts.

entry	catalyst	BET surface area (m^2/g)	pore volume (cm^3/g)	pore size (nm)
1	NiO_x@BCNTs	314	0.52	5.24
2	NiO_x@NC-800	318	0.48	5.36
3	NiO_x@NC-900	217	0.33	5.39
4	NiO_x@NC-1000	197	0.31	5.73

Table S3. Ni, NiO and N contents of the catalysts.

entry	catalyst	Ni/%	NiO/%	N %[b] (atomic%)
1	NiO_x@BCNTs	36.2	63.8	3.58
2	NiO_x@NC-800	32.8	67.2	3.32
3	NiO_x@NC-900	24.3	75.7	2.78
4	NiO_x@NC-1000	11.6	88.4	4.66
5	H_2-TPR-400[a]	37.0	63.0	--
6	H_2-TPR-550[a]	46.2	53.8	--
7	H_2-TPR-650[a]	50.7	49.3	--
8	H_2-TPR-750[a]	56.6	43.4	--
9	H_2-TPR-850[a]	62.6	37.4	--

[a] NiO_x@BCNTs was treated via H_2-TPR process under different temperature.
[b] The atomic percentage of N calculated from XPS data.

Table S4. Summary of the recently reported solid-state HER catalysts in basic electrolytes.

Catalyst	η-j[b]	TS[c]	Stability	Electrolyte solution	Reference
NiO_x@BCNTs (~0.40 mg cm^{-2})[a]	**183-10**	**119**	**10 h**	**1 M KOH**	**This work**
NiO_x@BCNTs (~3.18 mg cm^{-2})[a]	**79-10** **181-30**				
CoO_x@CN	232-10	115	1.67 h	1 M KOH	*J. Am. Chem. Soc.* **2015**, *137*, 2688
Ni-Mo-alloy on Ti foil	~80-10	--	100 h	1 M NaOH	*ACS Catal*. **2013**, *3*, 166
Co-NRCNTs	370-10	69	10 h	1 M KOH	*Angew. Chem. Int. Ed.* **2014**, *53*, 4372
NiO/Ni-CNT	<100-10	82	2 h	1 M KOH	*Nat. Commun.* **2014**. *4695*
Ni	400-10	--	--	1 M KOH	*Angew. Chem. Int. Ed.* **2012**, *51*, 12703
Ni/MWCNT	~350-10	102	--	1 M KOH	*J. Power Sources* **2014**, *266*, 365
MnNi	360-10	--	2 h	1 M KOH	*Adv. Funct. Mater.* **2015**, 25, 393
Ni-NiO/N-rGO	160	46	11.1 h	1 M KOH	*Adv. Funct. Mater.* **2015**, *25*, 5799
Ni@C NSs	270	143	12 h	1 M KOH	*J. Mater. Chem. A* ,**2016**, *4*,7297
Ni-G	75-1	182	1 h	0.1 M KOH	*Int. J. Hydrogen Energy*, **2016**, *41*, 3786
NiP nanospheres	434-50	122	11.1 h	1 M NaOH	*Int. J. Hydrogen Energy*, **2016**, *41*, 20515
Ni-S/CeO_2	170-30	165.6	--	1 M NaOH	*Int. J. Hydrogen Energy*, **2016**, *41*, 20485

[a] The loading mass was based on the mass of nickel.
[b] η (mV) stands for the overpotential at current density of j (mA cm^{-2}).
[c] TS represents Tafel slope (mV dec^{-1}).

Table S5. Exchange current density of the catalysts.

entry	catalyst	Exchange current density / mA cm^{-2}
1	NiO_x@BCNTs	0.308
2	NiO_x@NC-800	0.214
3	NiO_x@NC-900	0.212
4	NiO_x@NC-1000	0.171

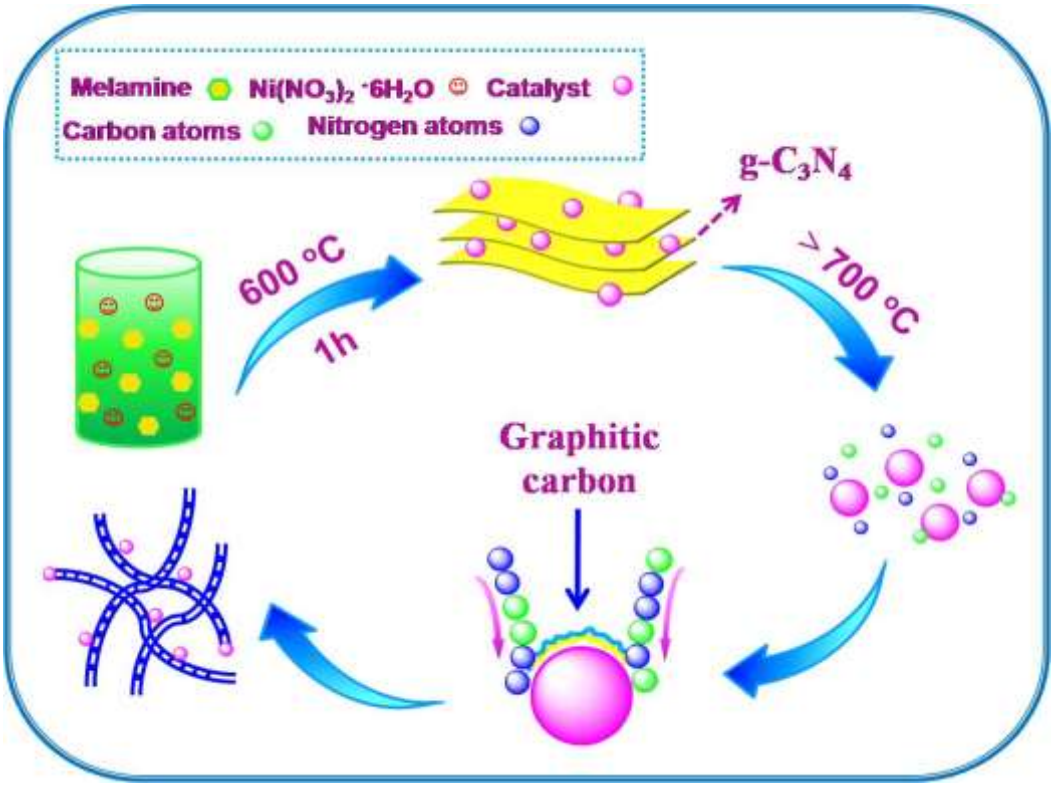

Scheme S1. Scheme for the fabrication of NiO_x@BCNTs.

In our case, thermal condenstion of melamine formed layered graphitic carbon nitride (g-C_3N_4) at low-temperature zone (<600 ^oC).[1] The Ni species were partially reduced to metallic Ni NPs by reductive groups decomposed from g-C_3N_4 as the the temperature rises. On the other hand, the g-C_3N_4 also acted as precursor to deposit nitrogen-doped carbon around the Ni NPs.[2] A high pyrolysis temperature or long holding period probably resulted in a sufficient decomposition of g-C_3N_4, and thus high concentrations of nitrogen and carbon fragments around the Ni NPs, which promoted the growth of nitrogen-doped carbon nanotubes. As a consequence, the Ni NPs were encapsulated in nitrogen-doped carbon shells. The experiment results show that controlled parameter in the experiment can lead to the production of BCNTs.

$$H_2O + e^- \longrightarrow H_{ads} + OH^- \quad \text{(Volmer)} \quad (1)$$

$$H_{ads} + H_{ads} \longrightarrow H_2 \quad \text{(Tafel)} \quad (2)$$

$$H_2O + H_{ads} + e^- \longrightarrow H_2 + OH^- \quad \text{(Heyrovsky)} \quad (3)$$

Scheme S2. Hydrogen evolution reaction mechanism.

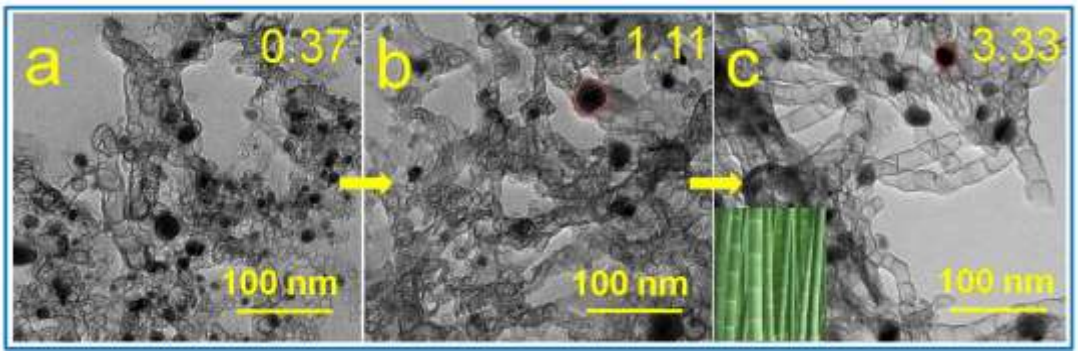

Figure S1. TEM images of samples with different $Ni(NO_3)_2 \cdot 6H_2O$ concentration calcinated at 800 ^oC, 1 h, a) 0.37 g, b) 1.11 g, c) 3.33 g.

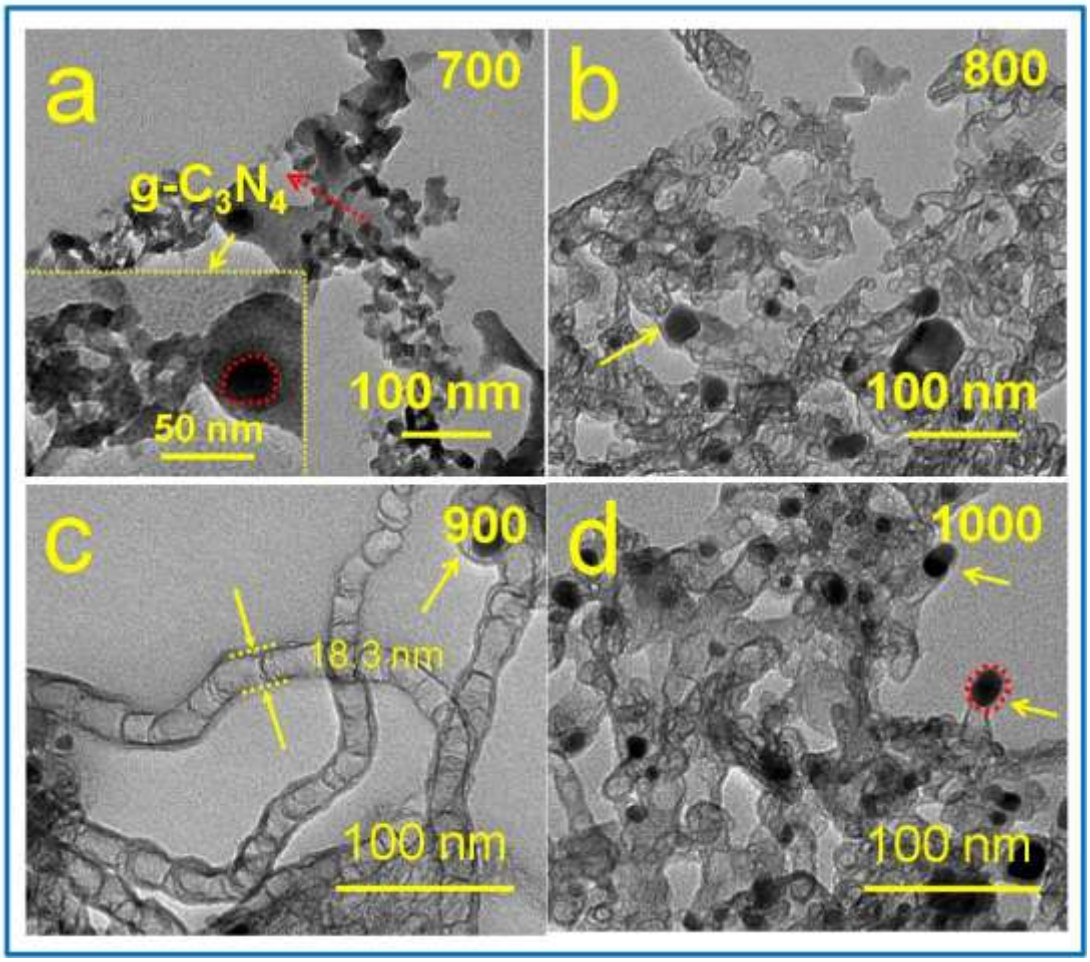

Figure S2. TEM images of samples with 1.11 g $Ni(NO_3)_2 \cdot 6H_2O$ calcinated at a) 700 ^oC, 1 h; b) 800 ^oC, 1 h; c) 900 ^oC, 1 h; d) 1000 ^oC, 1 h.

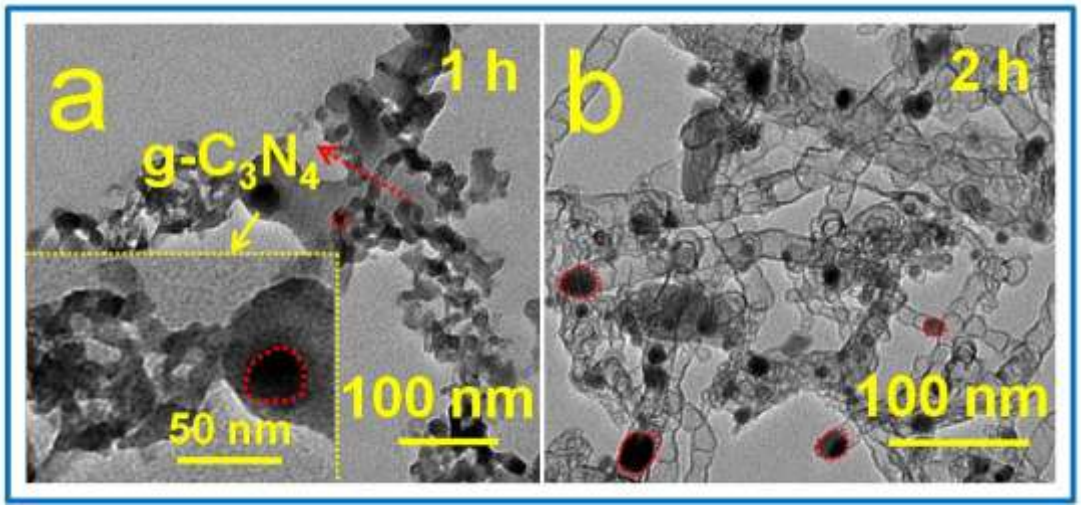

Figure S3. TEM images of samples with 1.11 g $Ni(NO_3)_2 \cdot 6H_2O$ calcinated at 700 ^oC with different holding time a) 1 h (NiO_x@NC-700), b) 2 h (NiO_x@BCNTs).

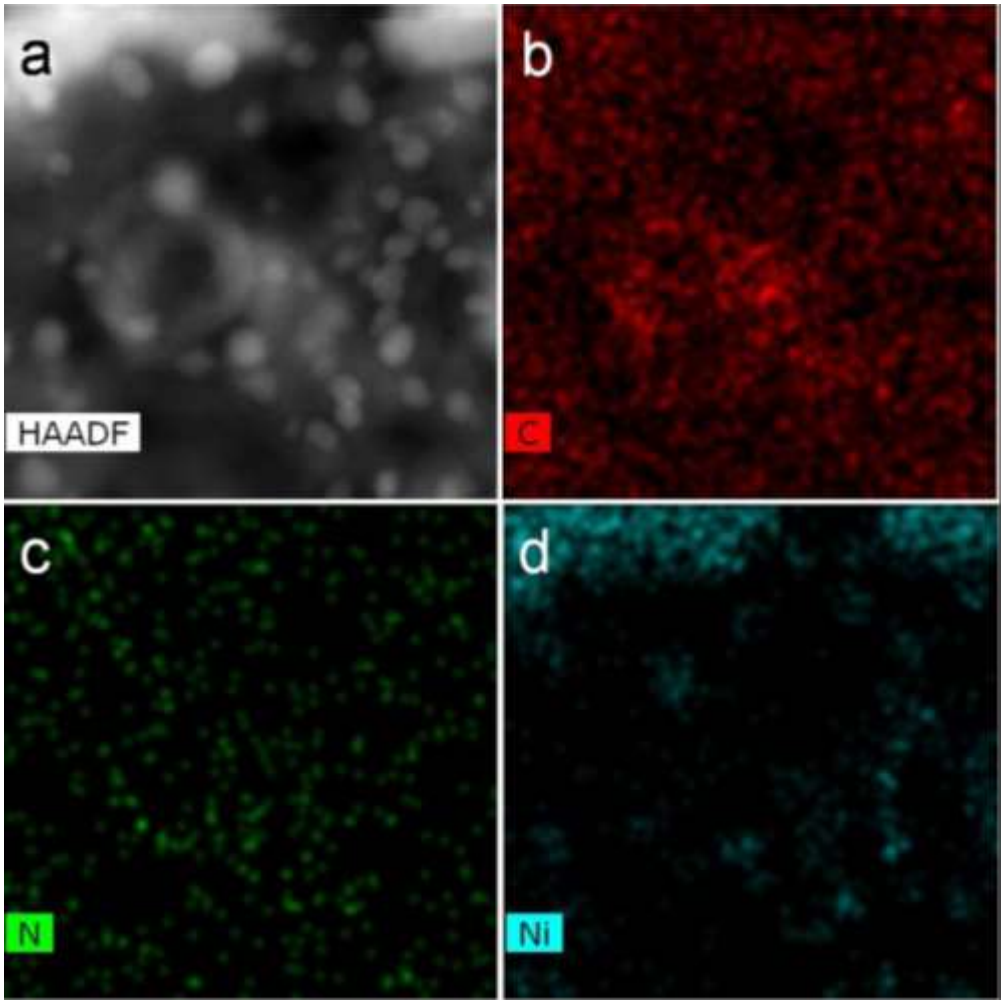

Figure S4. EDX elemental mapping of NiO_x@BCNTs.

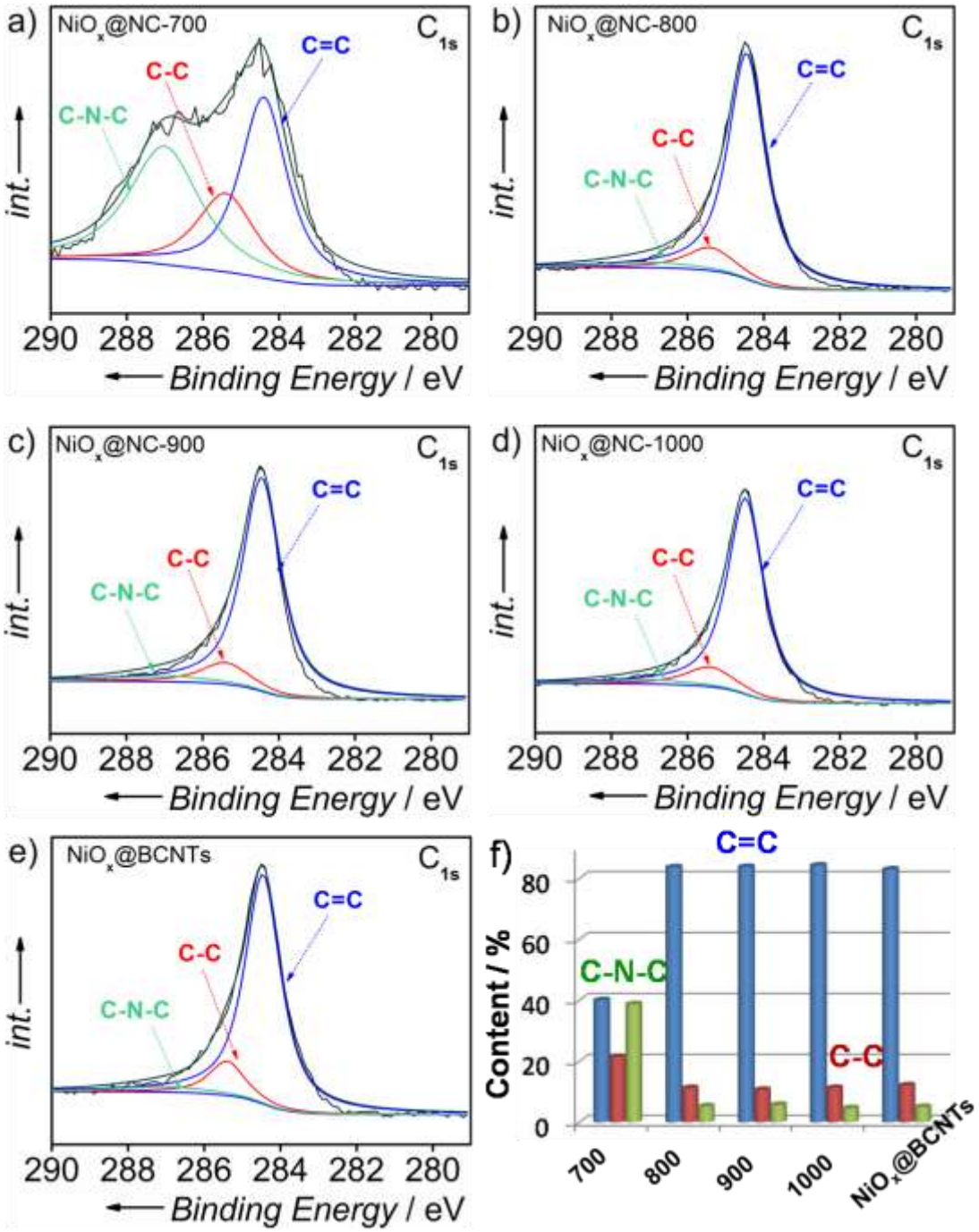

Figure S5. a, b, c, d, e) High-resolution C_{1s} XPS spectra of NiO_x@NC-700, NiO_x@NC-800, NiO_x@NC-900, NiO_x@NC-1000 and NiO_x@BCNTs. f) The content of the C=C, C-C and C-N-C species in products.

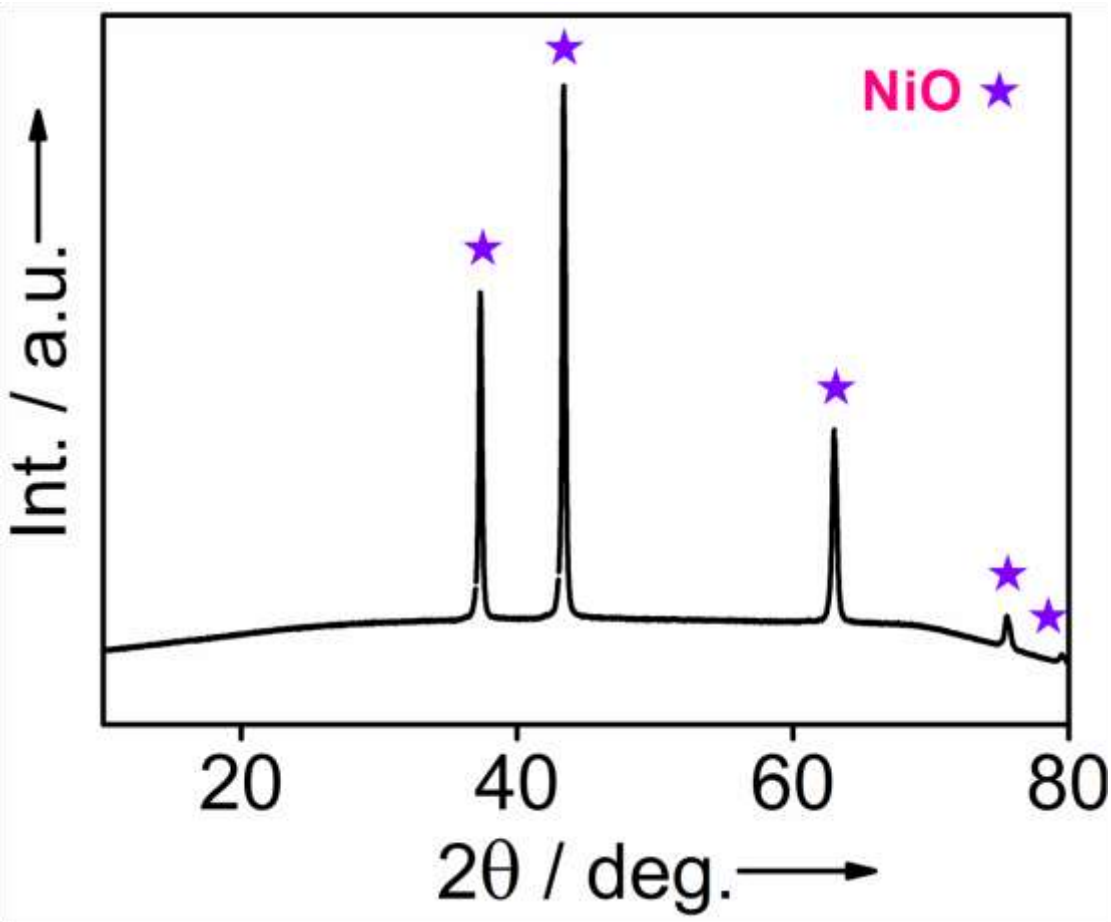

Figure S6. XRD of NiO calcinated at 800 ^{o}C for 1 h.

On the basis of XRD analysis (Figure S6), the characteristic peaks of contrast sample that directly calcinated $Ni(NO_3)_2 \cdot 6H_2O$ were assigned to NiO.

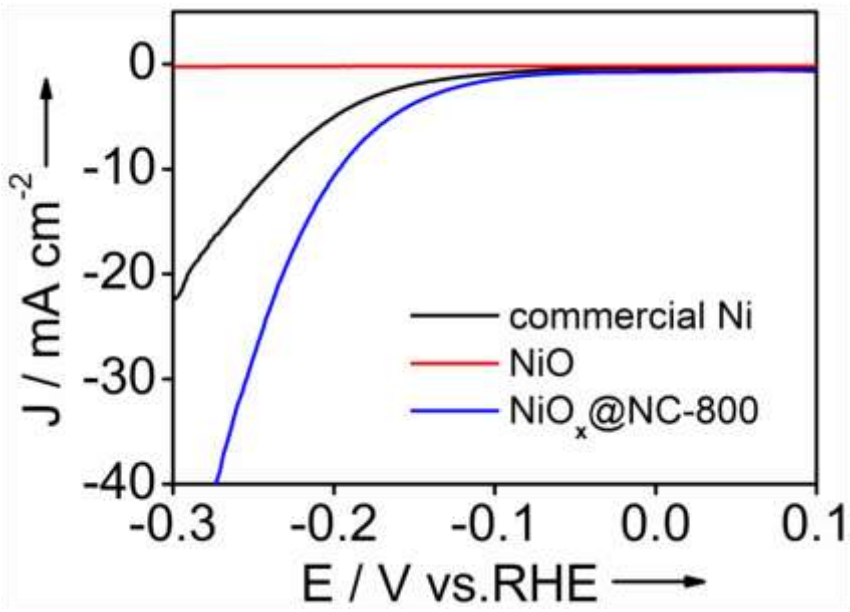

Figure S7. Polarization curves for control samples of commercial Ni, NiO and NiO_x@NC-800 in 1 M KOH.

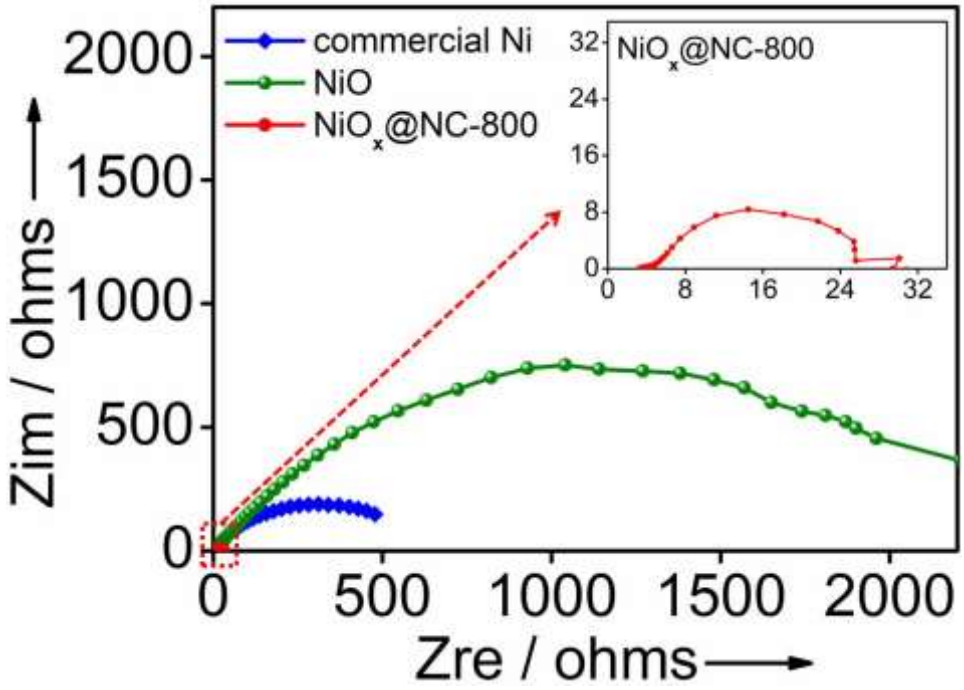

Figure S8. EIS spectra of commercial Ni, NiO and NiO_x@NC-800. The insert showed the enlarged EIS spectra of NiO_x@NC-800.

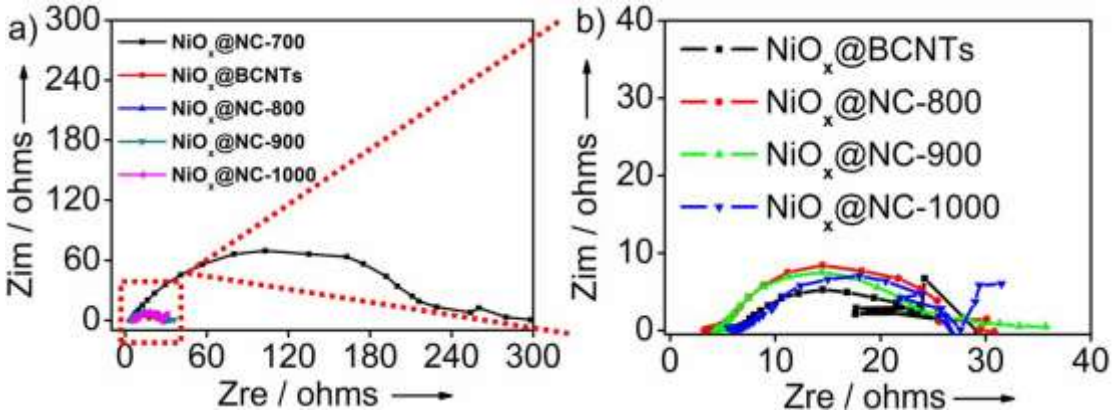

Figure S9. a) EIS spectra of samples calcinated at 700 ^{o}C, 1 h, 700 ^{o}C, 2h (NiO_x@BCNTs); 800 ^{o}C, 1 h; 900 ^{o}C, 1 h; 1000 ^{o}C, 1 h. b) The enlarged EIS spectra of samples NiO_x@BCNTs; 800 ^{o}C, 1 h; 900 ^{o}C, 1 h; 1000 ^{o}C, 1 h.

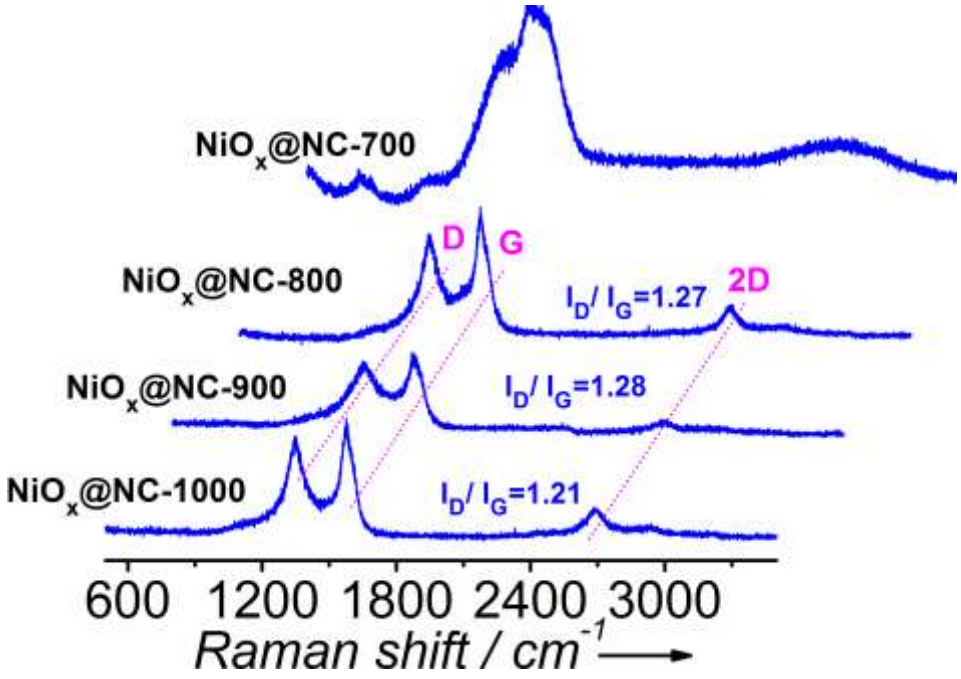

Figure S10. Raman spectra of samples calcinated at different temperatures, 1.11 g $Ni(NO_3)_2 \cdot 6H_2O$, 1 h.

On the basis of Raman data (Figure S10), the graphitization degrees of catalysts were determined by obtaining the ratio of intensities of the two bands (i.e., I_D/I_G). The I_D/I_G ratio of NiO_x@NC-800 (I_D/I_G=1.27) is similar to that of NiO_x@NC-900 (I_D/I_G=1.28), and NiO_x@NC-1000 (I_D/I_G=1.21).

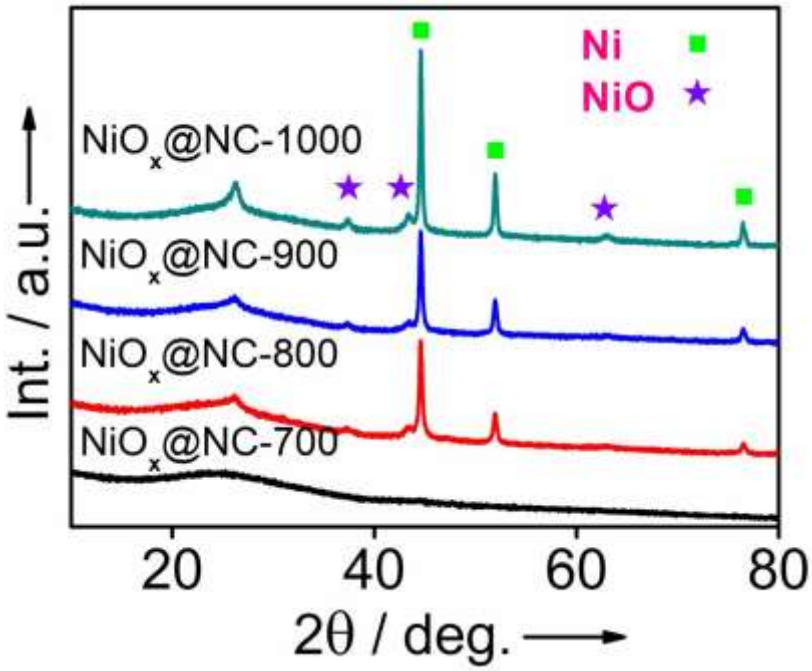

Figure S11. XRD of samples with 1.11 g $Ni(NO_3)_2 \cdot 6H_2O$ calcinated under different temperature for 1 h.

As shown in Figure S11, NiO_x@NC-700 only showed the diffraction peaks of graphite, owing to the formed Ni or NiO with lower crystallinity and smaller particle size under 700 ^oC.

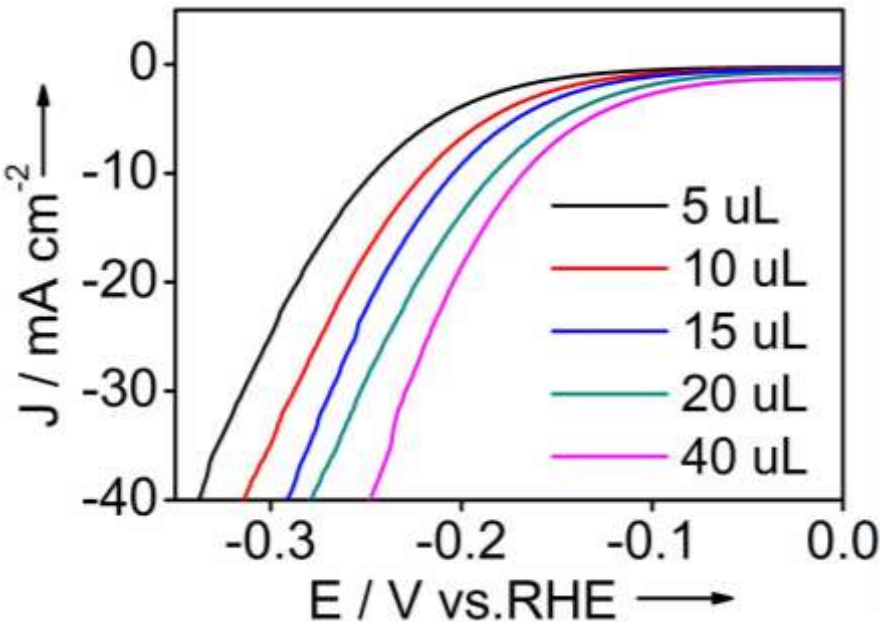

Figure S12. Polarization curves of NiO_x@BCNTs in 1 M KOH with different loading mass.

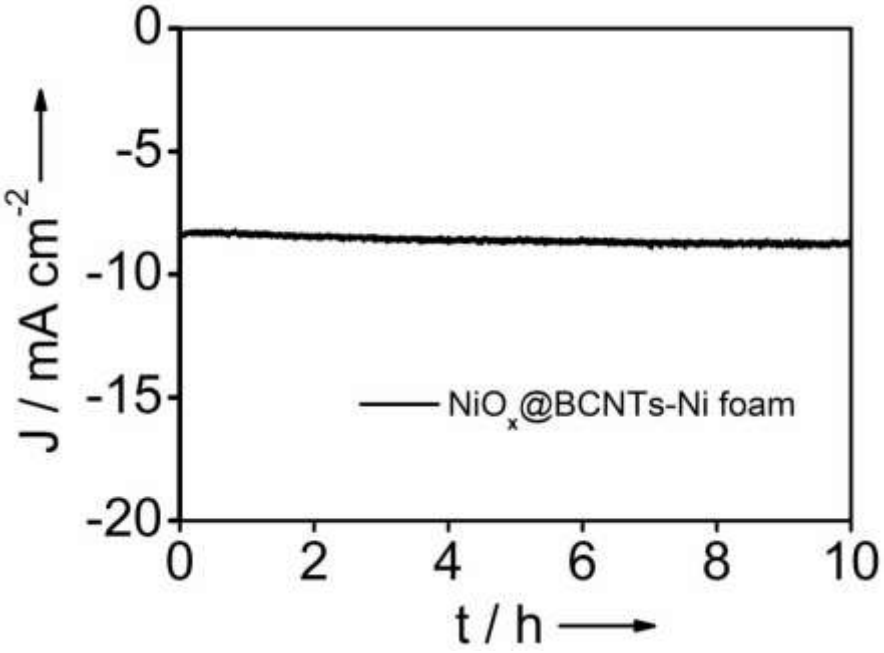

Figure S13. Chronoamperometric response of NiO_x@BCNTs-Ni foam. The corresponding LSV data in Figure 3b was obtained after i-t test.

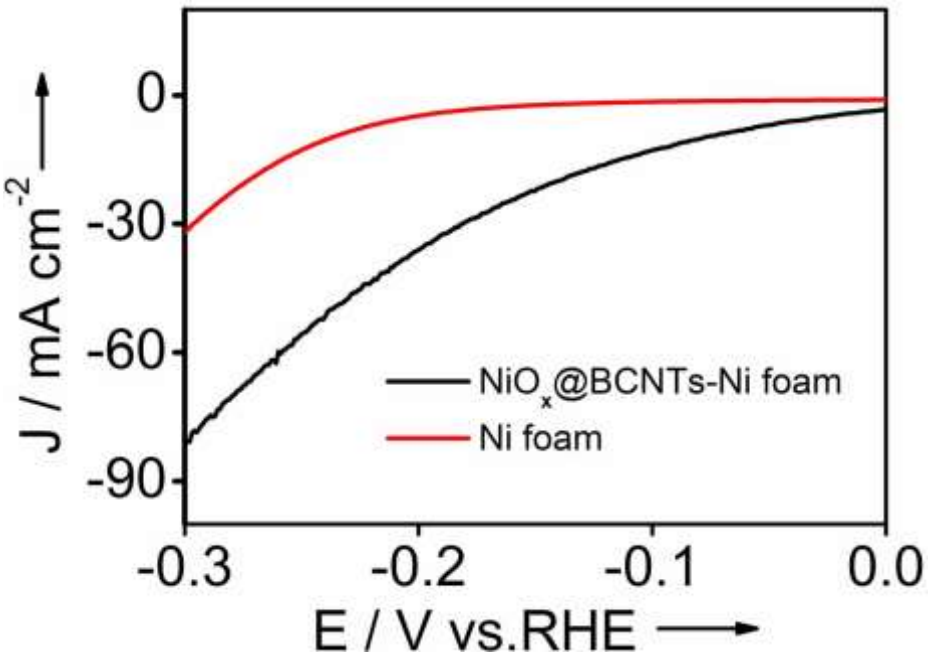

Figure S14. LSV curves of NiO_x@BCNTs on Ni foam and Ni foam.

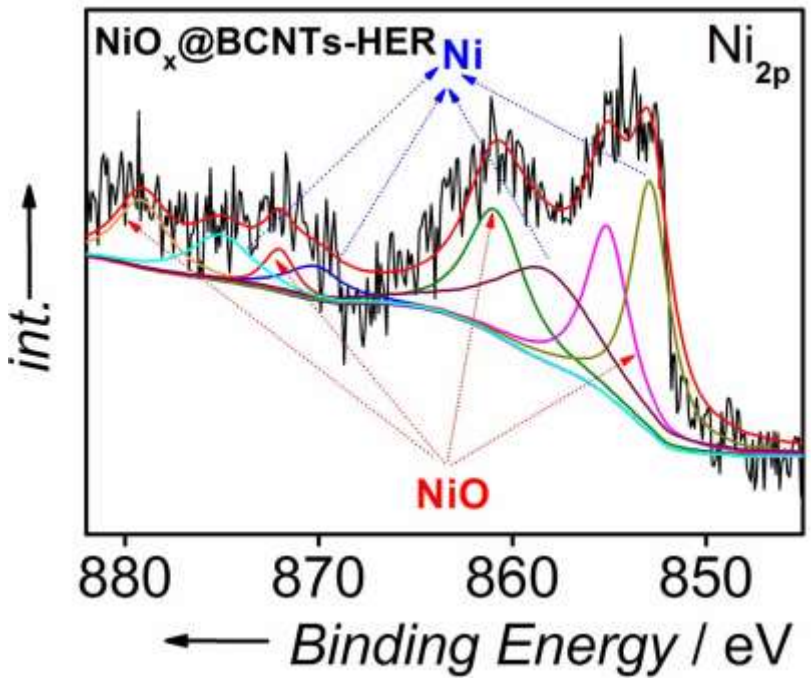

Figure S15. High-resolution Ni_{2p} XPS spectra of NiO_x@BCNTs-HER.

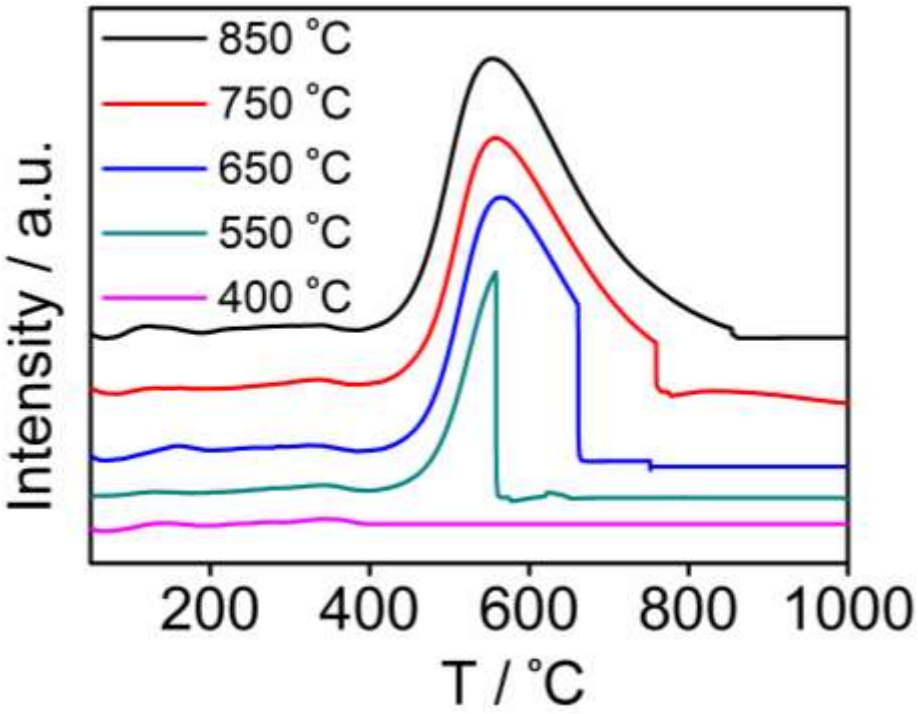

Figure S16. H_2-TPR plots of NiO_x@BCNTs treated with different temperatures.

In order to prevent the H_2 to continue reducing NiO during the cooling process, we immediately switch H_2 to He after reaching the target final temperature. When there is no H_2 in the gas circuit, the curve will show a sudden change in signals.

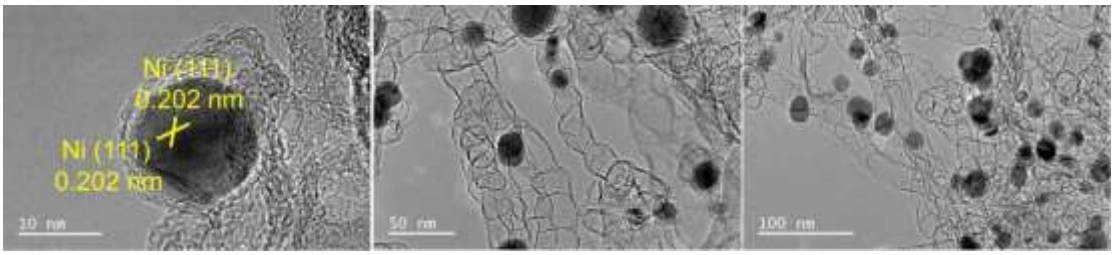

Figure S17. HRTEM images of NiO_x@BCNTs treated via H_2-TPR process under 400 ^oC.

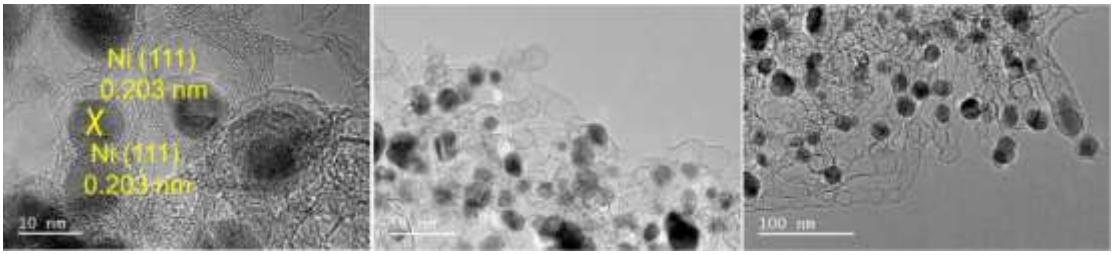

Figure S18. HRTEM images of NiO_x@BCNTs treated via H_2-TPR process under 550 ^oC.

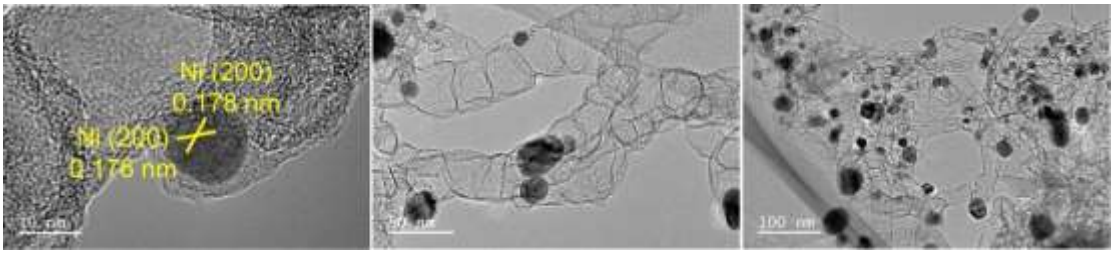

Figure S19. HRTEM images of NiO_x@BCNTs treated via H_2-TPR process under 650 ^oC.

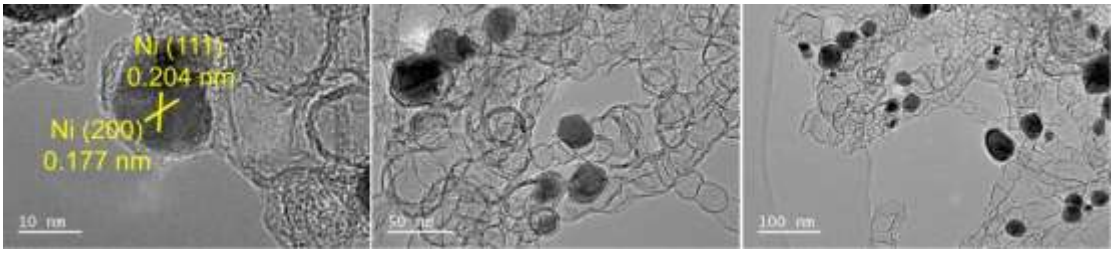

Figure S20. HRTEM images of NiO_x@BCNTs treated via H_2-TPR process under 750 ^oC.

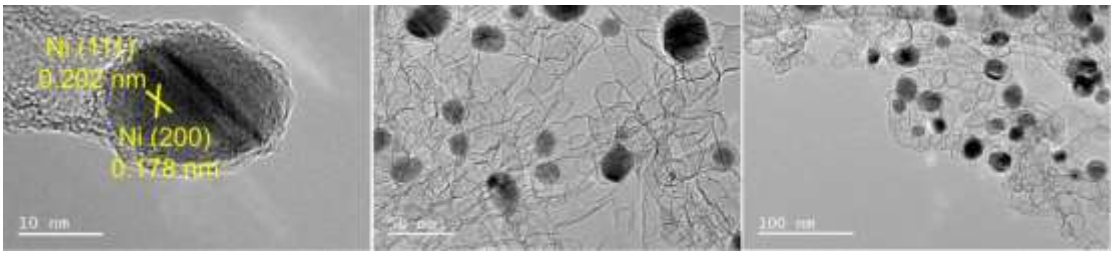

Figure S21. HRTEM images of NiO_x@BCNTs treated via H_2-TPR process under 850 ^oC.

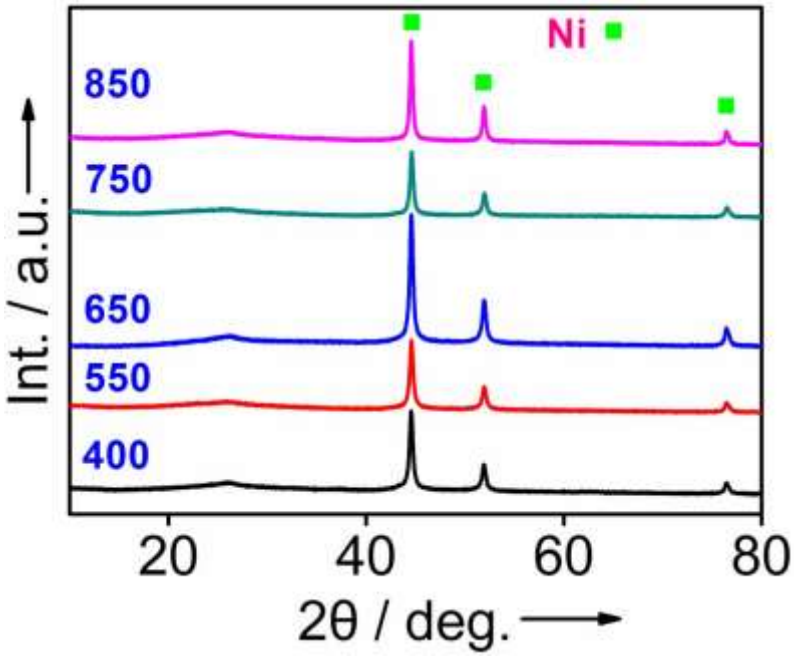

Figure S22. XRD patterns of NiO_x@BCNTs treated via H_2-TPR process under different temperature.

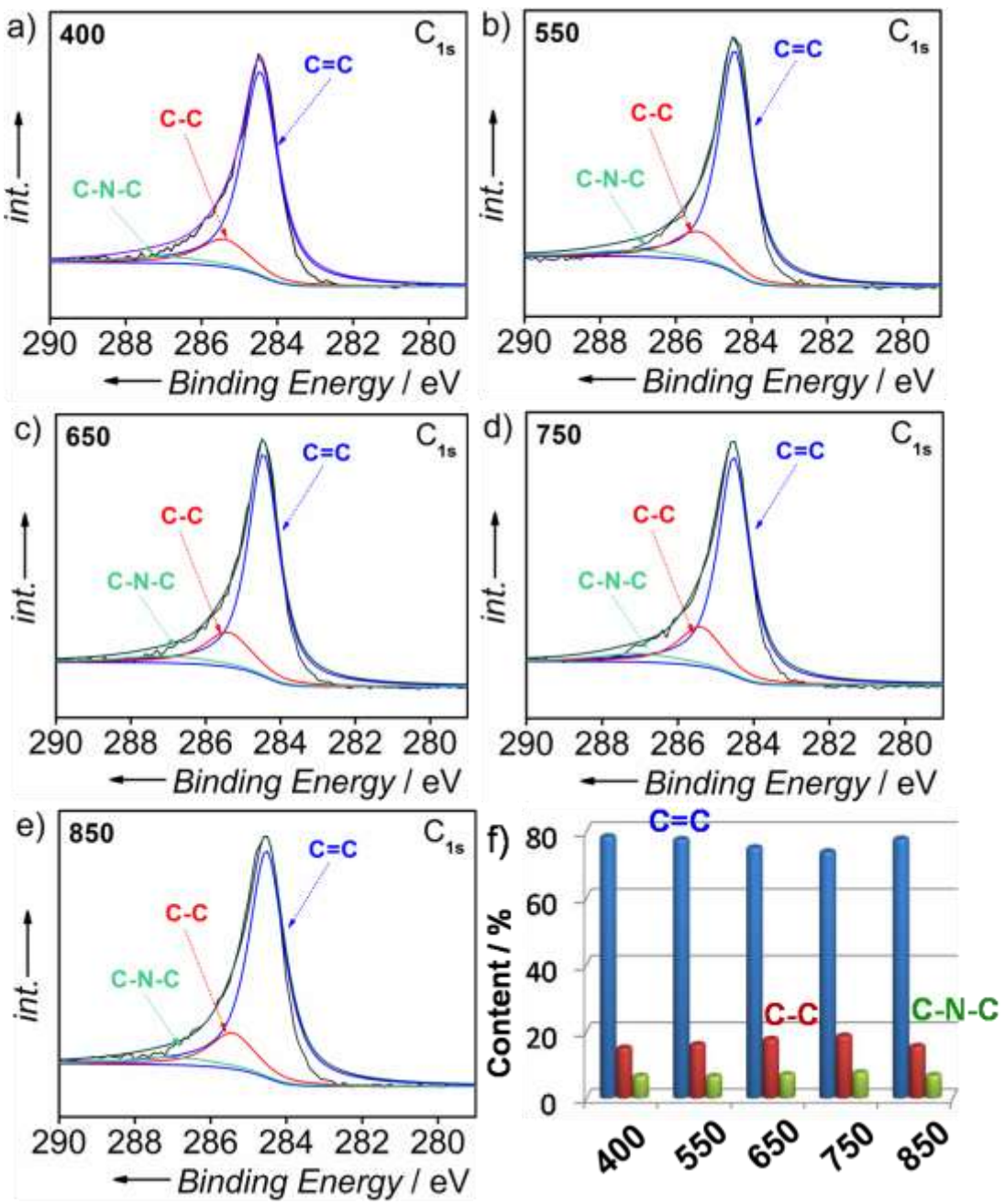

Figure S23. a, b, c, d, e) High-resolution C_{1s} XPS spectra of NiO_x@BCNTs treated via H_2-TPR process under different temperature. f) The content of the C=C, C-C and C-N-C species in products.

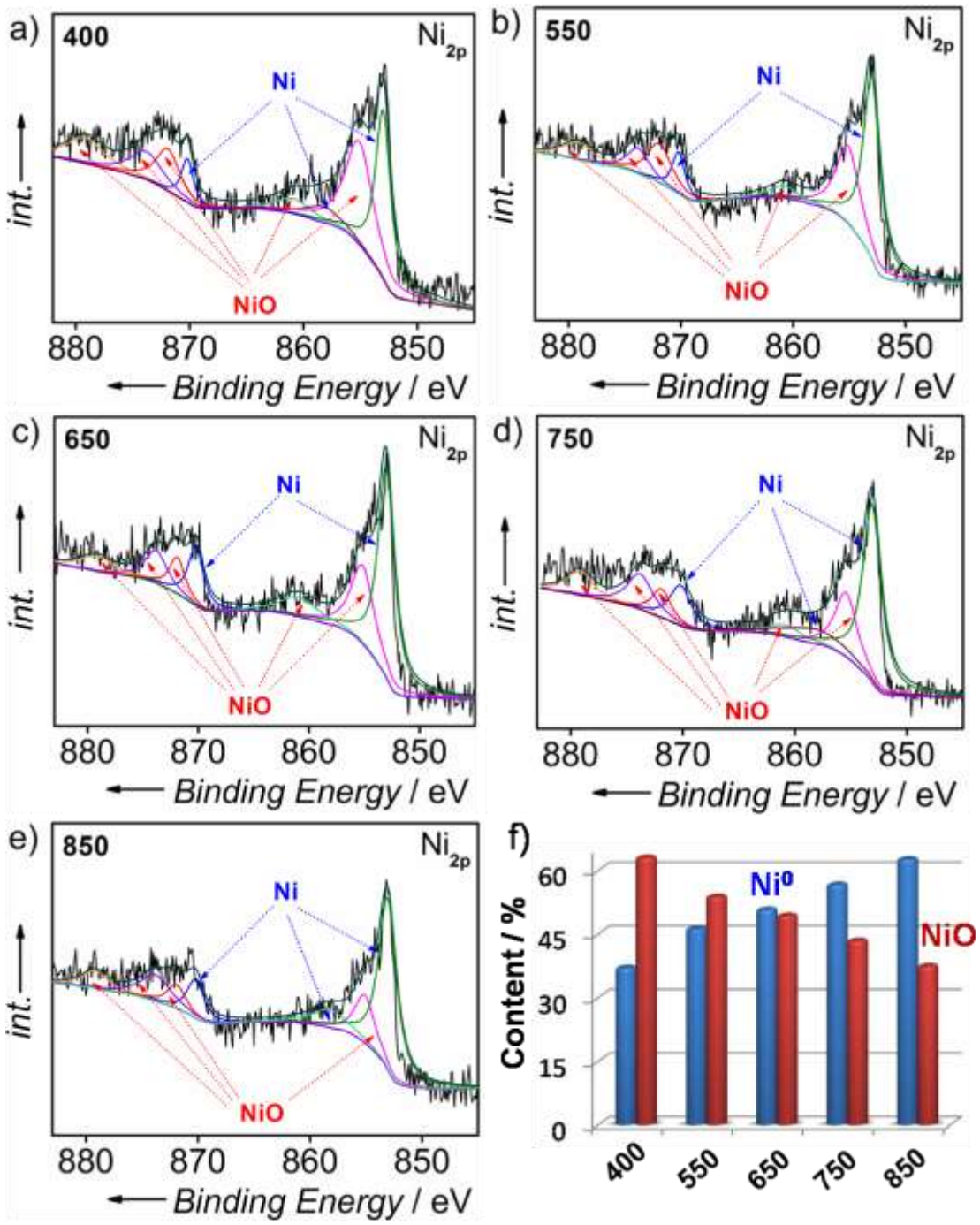

Figure S24. a, b, c, d, e) High-resolution Ni_{2p} XPS spectra of NiO_x@BCNTs treated via H_2-TPR process under different temperature. f) The content of the Ni and NiO species in products.

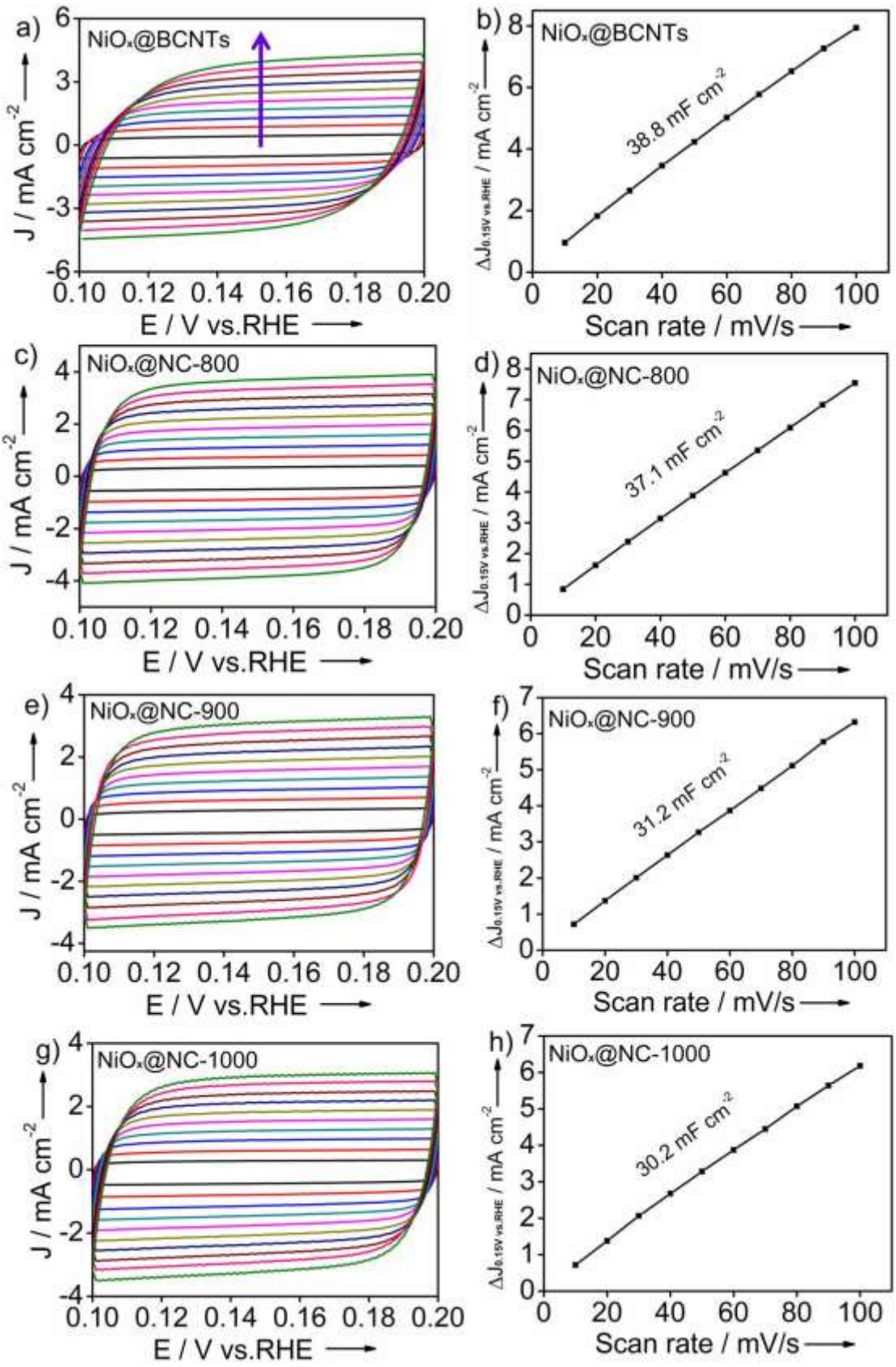

Figure S25. a, c, e, g) Cyclic voltammetry curves of NiO_x@BCNTs, NiO_x@NC-800, NiO_x@NC-900 and NiO_x@NC-1000, respectively, at different scan rates under

overpotential from 0.1 to 0.2 V (vs.RHE). The purple arrow indicates the scan rate from 10 mV to 100 mV. b, d, f, h) The differences in current density variation (ΔJ=Ja-Jc) at an overpotential of 0.15 V plotted against scan rate fitted to a linear regression enables the estimation of C_{dl}, where the slope is twice C_{dl}.

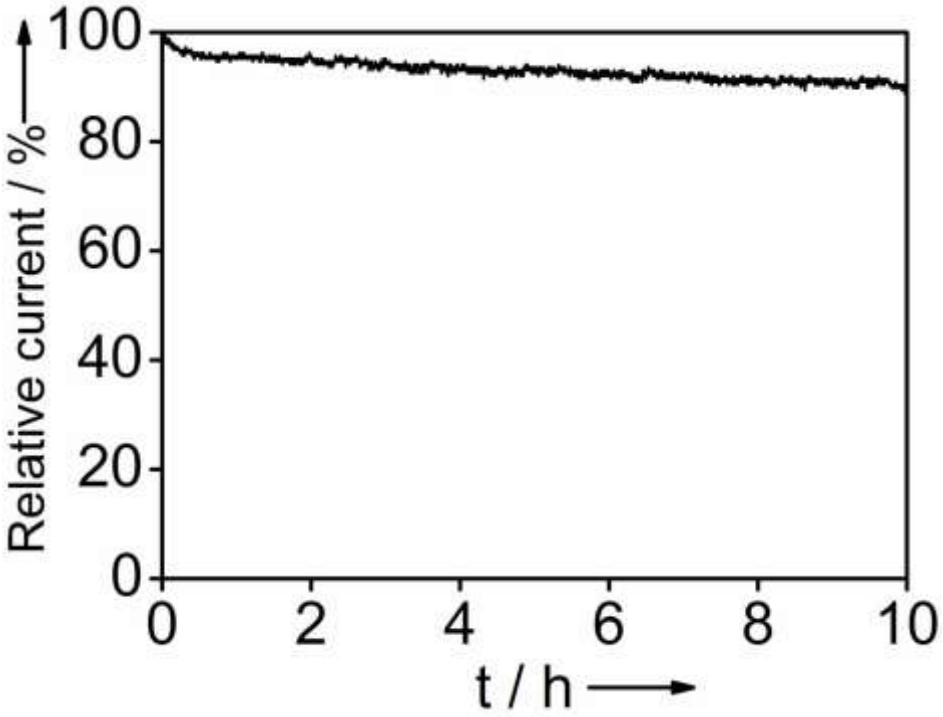

Figure S26. Current-time (i-t) chronoamperometric response of NiO_x@BCNTs in 1 M KOH.

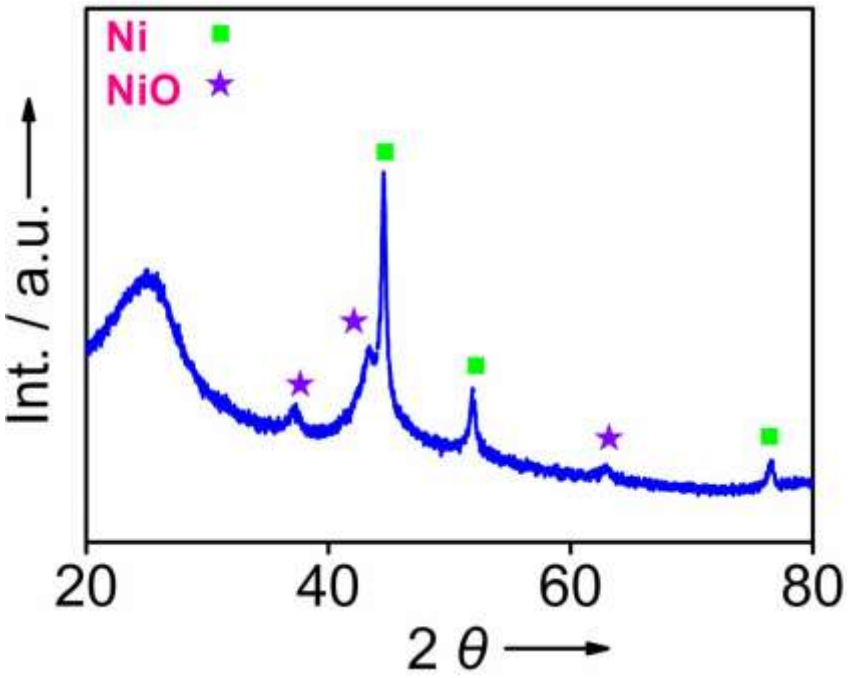

Figure S27. XRD patterns of NiO_x@BCNTs after long-term HER test.

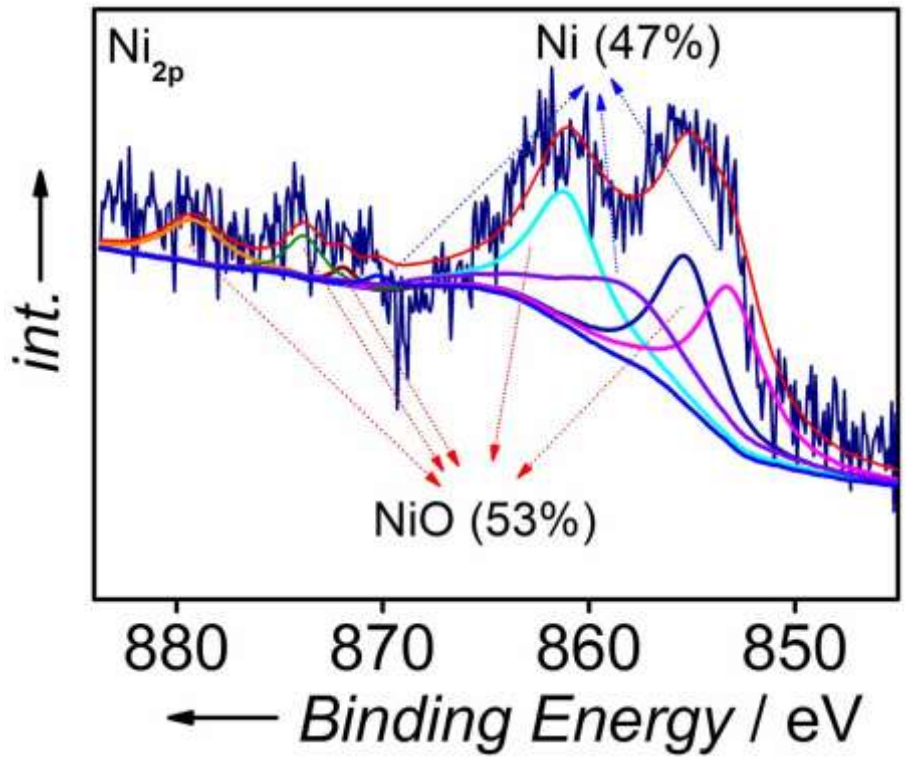

Figure S28. High-resolution Ni_{2p} XPS spectra of NiO_x@BCNTs after long-term HER test.

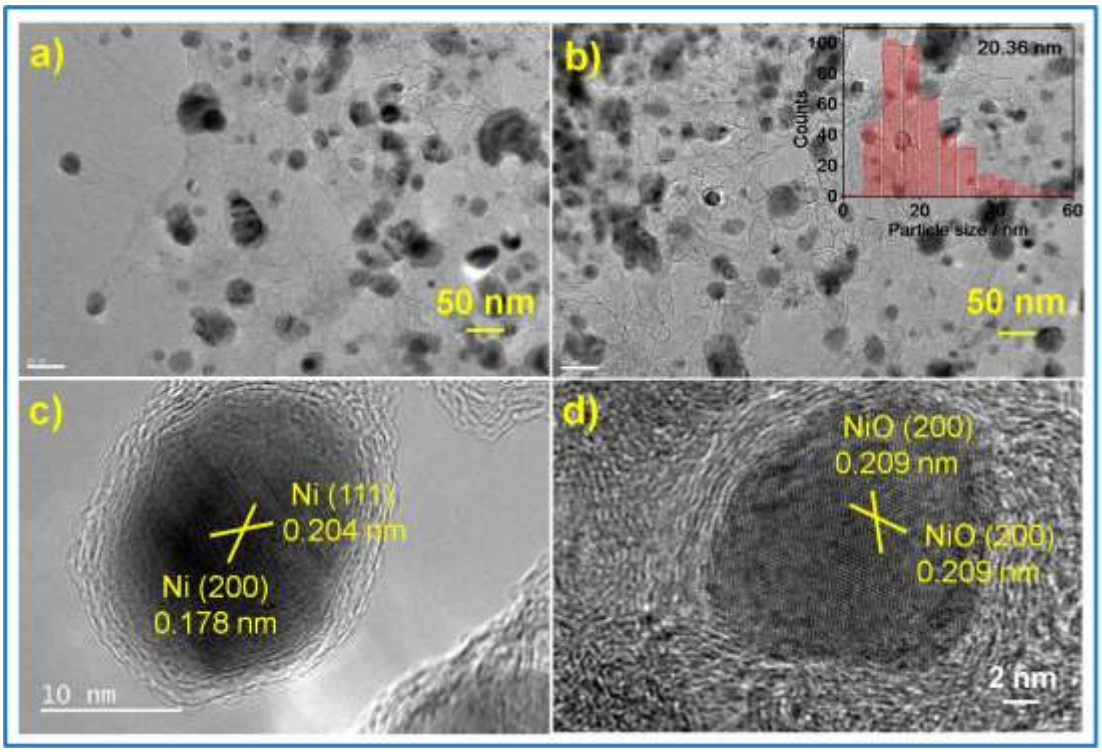

Figure S29. TEM and HRTEM images of NiO_x@BCNTs after long-term HER test

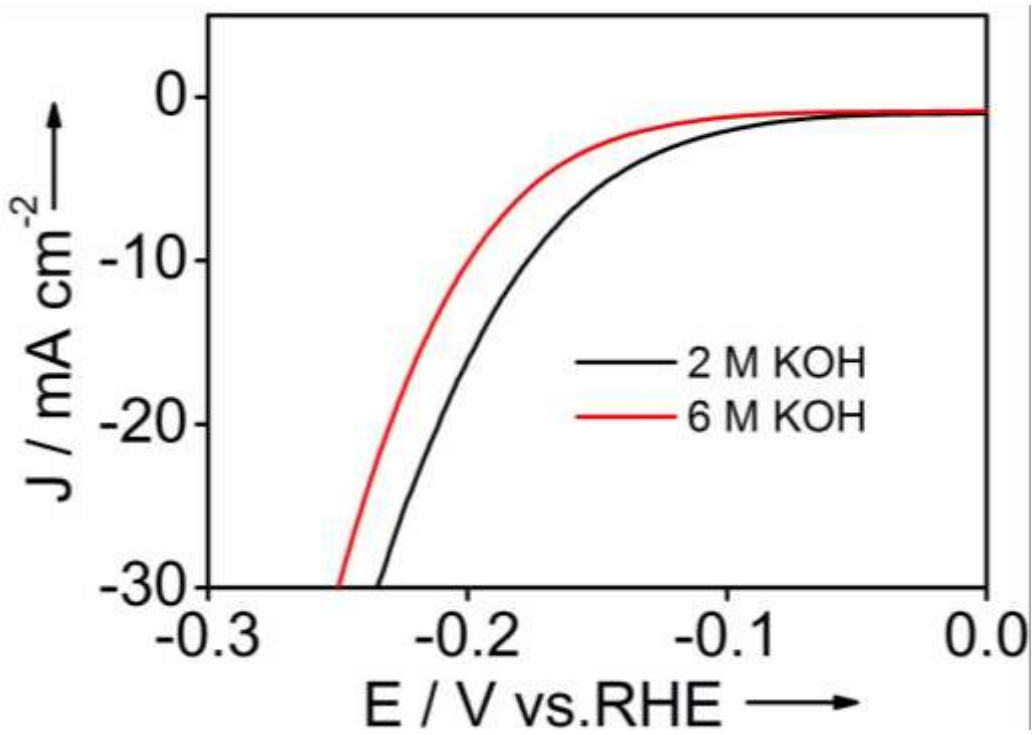

Figure S30. Polarization curves of NiO_x@BCNTs in 2 M KOH and 6 M KOH.

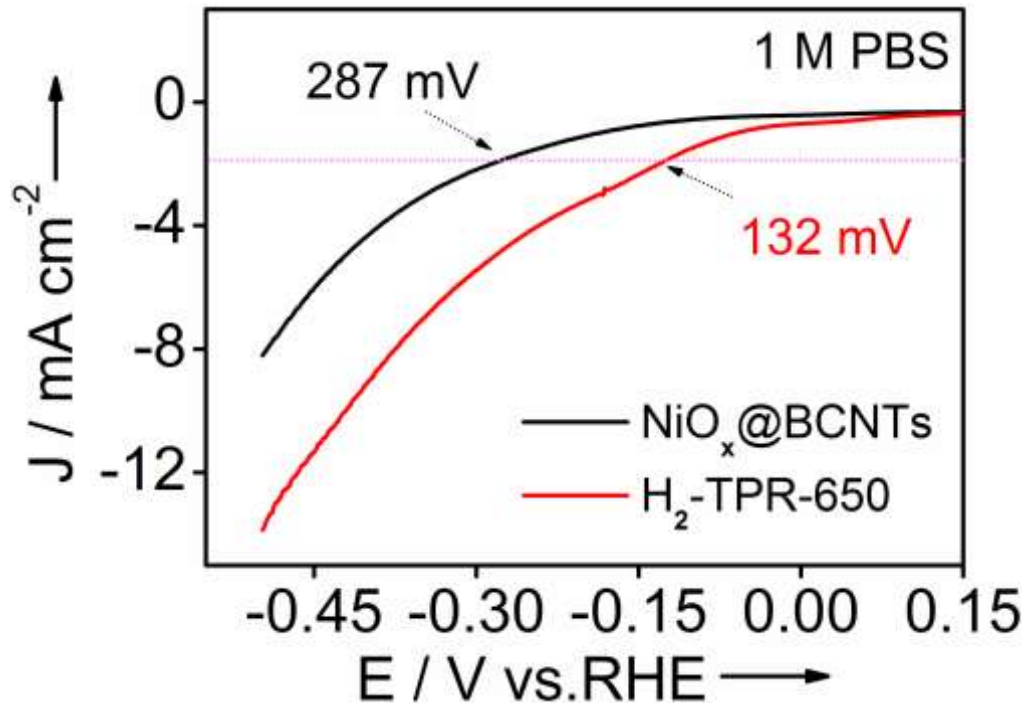

Figure S31. Polarization curves of NiO_x@BCNTs and H_2-TPR-650 in 1 M PBS.

Computational section

Calculations were performed by using periodic, spin-polarized DFT as implemented in Vienna ab initio program package (VASP).[3-4] The electron-ion interactions were described by the projector augmented wave (PAW) method proposed by Blöchl[5] and implemented by Kresse.[6] PBE functional[7] was used as

exchange-correlation functional approximation and a plane wave basis set with an energy cutoff of 400 eV was chosen. A p (6×6) four-layer slab with (1 1 1) surface cleavaged was modeled as the active surface for the inherent Ni^0. As for the Ni/NiO interface model, a p (5×5) four-layer (1 1 1) NiO slab was embedded under one p (6 ×6) single layer (1 1 1) Ni^0 slab (see Figure S32). Only gamma k-point is used for the Brillouin zone sampling for these two models. A p (3×3) four-layer NiO slab with (100) surface was modeled for bulk NiO since this face is most stable.[8] A (2×2×1) k-point sampling is used for NiO model to ensure accuracy. Hubbard-U correction (DFT+U method)[9] was applied to improve the description of localized Ni d-electrons for Ni^0/NiO interface model. A value of U = 6.3 eV was set since this value is considered reasonable.[10-11] The bottom two layers were kept fixed during the structure optimization. Only gamma k-point is used for the Brillouin zone sampling. The periodic condition is employed along the x and y direction. The vacuum space along the z direction was set to be 15 Å. The relaxation is stopped when the force residue on the atom is smaller than 0.02 eV/Å. The hydrogen binding energy is defined using the equation:[12]

$$E^{H}_{atomic} = E_{H-slab} - E_{slab} - 0.5 \times E_{H_2(g)}$$

where E^{H}_{atomic} is the binding energy of atomic hydrogen on the given slab, E_{H-slab} is the energy of the slab with one hydrogen adsorbed, E_{slab} is the energy of the slab in a vacuum, and $E_{H2(g)}$ is the energy of hydrogen in the gas phase.

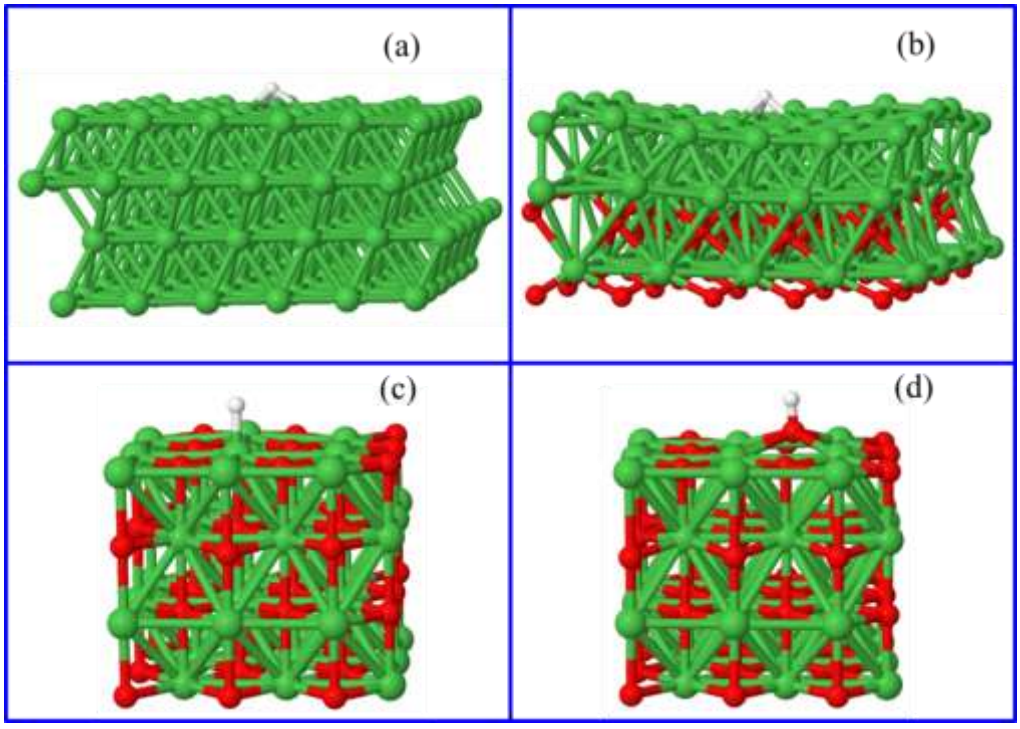

Figure S32. Hydrogen binding on (a) inherent Ni^0 (111); (b) Ni/NiO (111) interface; (c) Ni site of NiO(100); (d) O site of NiO (100). Cyan: nickel; red: oxygen; white: hydrogen.

Reference

(1) Wang, Y.; Wang, X.; Antonietti, M. Polymeric Graphitic Carbon Nitride as a Heterogeneous Organocatalyst: From Photochemistry to Multipurpose Catalysis to Sustainable Chemistry. *Angew. Chem., Int. Ed.* **2012,** *51*, 68-89.

(2) Duan, J. J.; Chen, S.; Jaroniec, M.; Qiao, S. Z. Porous C_3N_4 Nanolayers@N-Graphene Films as Catalyst Electrodes for Highly Efficient Hydrogen Evolution. *ACS Nano* **2015,** *9*, 931-940.

(3) Kresse, G.; Furthmüller, J. Efficiency of Ab-initio Total Energy Calculations for Metals and Semiconductors Using a Plane-wave Basis Set. *Comput. Mater. Sci.* **1996,** *6*, 15-50.

(4) Kresse, G.; Furthmüller, J. Efficient Iterative Schemes for Ab Initio Total-energy Calculations Using a Plane-wave Basis Set. *Phys. Rev. B* **1996,** *54*, 11169-11186.

(5) Blöchl, P. E. Projector Augmented-wave Method. *Phys. Rev. B* **1994,** *50*, 17953-17979.

(6) Kresse, G.; Joubert, D. From Ultrasoft Pseudopotentials to the Projector Augmented-wave Method. *Phys. Rev. B* **1999,** *59*, 1758-1775.

(7) Perdew, J. P.; Burke, K.; Ernzerhof, M. Generalized Gradient Approximation Made Simple. *Phys. Rev. Lett.* **1996,** *77*, 3865-3868.

(8) Pacchioni, G.; Di Valentin, C.; Dominguez-Ariza, D.; Illas, F.; Bredow, T.; Kluner, T.; Staemmler, V. Bonding of NH_3, CO, and NO to NiO and Ni-doped MgO: a Problem for Density Functional Theory. *J. Phys.: Condens. Matter* **2004,** *16*, S2497-S2507.

(9) Liechtenstein, A. I.; Anisimov, V. I.; Zaanen, J. Density-functional Theory and Strong Interactions: Orbital Ordering in Mott-Hubbard Insulators. *Phys. Rev. B* **1995,** *52*, R5467-R5470.

(10) Rohrbach, A.; Hafner, J.; Kresse, G. Molecular Adsorption on the Surface of Strongly Correlated Transition-metal Oxides: A Case Study for CO/NiO(100). *Phys. Rev. B* **2004,** *69*, 075413-1-075413-13.

(11) Rohrbach, A.; Hafner, J. Molecular Adsorption of NO on NiO(100): DFT and DFT+U Calculations. *Phys. Rev. B* **2005,** *71*, 045405-1-045405-7.

(12) Nørskov, J. K.; Bligaard, T.; Logadottir, A.; Kitchin, J. R.; Chen, J. G.; Pandelov, S.; Stimming, U. Trends in the Exchange Current for Hydrogen Evolution. *J. Electrochem. Soc.* **2005,** *152*, J23-J26.